Toroidal Dipole-Induced Photocurrent Enhancement in Si Nanodisk Hexagonal Array below the Band Gap

Hasebe, Hiroaki
Moriasa, Keisuke
Yamashita, Kaito
Sugimoto, Hiroshi
Fujii, Minoru

(Citation)
ACS Photonics,9(10):3302-3309

(Issue Date)
2022-10-19

(Resource Type)
journal article

(Version)
Accepted Manuscript

Toroidal dipole-induced photocurrent enhancement in Si nanodisk hexagonal array below the band gap

Hiroaki Hasebe,[†] Keisuke Moriasa,[†] Kaito Yamashita,[†] Hiroshi Sugimoto,[†,‡] Minoru Fujii[†]

[†]Department of Electrical and Electronic Engineering, Graduate School of Engineering, Kobe University, Rokkodai, Nada, Kobe 657-8501, Japan

[‡]JST-PRESTO, Honcho 4-1-8, Kawaguchi, Saitama 332-0012, Japan

KEYWORDS. Toroidal dipole, dielectric nanodisk, absorption enhancement, photocurrent, sensing

ABSTRACT

A hexagonal array of low-aspect-ratio silicon nanodisks is formed on a silicon thin film and the optical absorption and photocurrent properties are studied. Numerical simulations reveal that the nanodisk array possesses the toroidal dipole modes that tightly confine incoming light in a silicon region below the nanodisks. The field confinement brings about narrow-band absorption when the extinction coefficient (κ) is very small, e.g., $\kappa = 10^{-2} \sim 10^{-3}$. This suggests that defect-related sub-band gap absorption of silicon can be enhanced by utilizing the modes. Transmittance spectra of fabricated devices reveal that narrow dips assigned to the toroidal dipole resonances appear in the sub-band gap region. At the resonance wavelengths, the photocurrent is substantially enhanced;

the enhancement factor reaches 30-fold. The observed narrow-band photodetection can be used as a current-detection-type refractive index sensor operating in the near infrared range.

Introduction

Near infrared (NIR) light often defined in the wavelength range of 800 – 2500 nm is transparent in many materials and has been widely used in optical telecommunication[1–4], face recognition[5,6], autonomous driving, gas sensing[7], bio imaging[8–10], etc. Conventional silicon (Si) photodetectors have sensitivity up to ~1100 nm, and longer wavelength ranges are covered by narrow band gap semiconductors such as InGaAs, InP, and Ge. Photodetectors of these narrow band gap semiconductors have been monolithically integrated on a Si device either by a transfer process or direct crystal growth on Si. The integration extends the operation range of Si-based photodetection devices to 1700 nm or to even longer wavelengths.

Recently, new technologies to extend the detection range of Si-based photodetection devices below the band gap have been emerging. The most extensively studied one is utilizing internal photoemission at a Schottky junction between Si and a noble metal nanoantenna[11–14]. Incoming light is absorbed by the excitation of localized surface plasmon resonances (LSPRs) in a noble metal nanoantenna. Decaying of surface plasmons to hot electrons having energies larger than the Schottky barrier height, and injection of the hot electrons to Si generates photocurrent. Since the resonance wavelength of LSPRs can be controlled in a wide range by the aspect ratio of a nanoantenna[15], the devices can detect photons up to 1600 nm without using narrow band gap semiconductors[11]. Similar devices using noble metal nanogratings and surface plasmon polaritons are also developed.[12–14]A problem of the Schottky junction approach is the limited choice of noble metal. A metal nanoantenna has to have the LSPR in the NIR range and has to make a good

Schottky contact with Si. Practically, Au is a sole choice to satisfy these criteria. However, Au is not a preferable material for a conventional CMOS process.

Another approach to extend the detection range of Si-based devices is utilizing defect-mediated light absorption[16–21]. Introduction of defects in crystalline Si forms defect-related states in the band gap that can be used for light absorption in the sub-band gap wavelength range. However, since absorption by defect-related states is very small, it should be enhanced by optical resonances of a photonic structure to achieve reasonable sensitivity of light detection. Several different approaches are proposed to enhance light absorption of Si and similar high-refractive index dielectric materials[22]. For example, narrow-band enhancement of photocurrent is observed below the band gap by utilizing Mie resonances (whispering gallery modes) of a few μm-size Si sphere as a nanoantenna.[19] According to the coupled mode theory, the absorptance of a single mode resonator is limited to 50% (critical coupling)[23,24]. Theoretically, near-unity absorption can be achieved if two modes such as electric dipole (ED) and magnetic dipole (MD) modes degenerate[22,24,25]. In arrays of amorphous Si nanoparticles, the absorptance as large as 0.83 is achieved by properly controlling the overlap of the ED and MD Mie resonances[26]. Degenerate critical coupling is also studied in the case of electric and magnetic quadrupole modes in a Si nanodisk array[27]. Another interesting approach for absorption enhancement is utilizing an anapole state, which is realized by destructive interference between cartesian ED and toroidal dipole (TD) modes[28,29]. In the anapole state, suppression of far field radiation results in field confinement in a nanostructure, which induces strong enhancement of light absorption[30,31], nonlinear optical responses[32–34], Raman scattering[35], photothermal effect[36], stimulated emission (lasing)[37], photocatalytic effects[38], and photoelectrode performance[39].

In this work, we exploit TD modes of Si nanodisks for the photocurrent enhancement in a Si metasurface in the sub-band gap wavelength range. In a previous work[31], we showed that a hexagonal array of low-aspect-ratio Si nanodisks exhibits sharp absorption peaks due to the toroidal dipole resonances. Because of the narrow-band absorption enhancement in a transparent range of Si, the metasurface is potentially useful for wavelength-selective photodetection in the sub-band gap wavelength range. In order to utilize the narrow-band absorption enhancement for the photocurrent enhancement, we produce a low-aspect-ratio Si nanodisk hexagonal array on a thin Si film that acts as a conductive layer for photocurrent detection. We first demonstrate by numerical simulations that nanodisks strongly confine the electric field of incident light in a Si thin film beneath them, and that the field confinement results in the narrow-band absorption enhancement. Simulations assuming different values of extinction coefficient reveal that, because of the non-radiating nature of the mode, the absorptance has the maximum at a very low extinction coefficient range, e.g., $\sim 10^{-3}$. This suggests notable photocurrent enhancement in the sub-band gap wavelength range. We experimentally demonstrate that formation of a Si nanodisk hexagonal array on a Si thin film enhances the photocurrent at most 30-fold at the wavelength of the absorption enhancement peaks, and that the peak wavelengths can be controlled by the Si thin film thickness. We also show that the produced device is potentially useful as a current-detection-type refractive index sensor because of the narrow photocurrent peaks.

Results and discussion

Numerical Simulations

We first calculate optical responses of Si nanodisk hexagonal arrays schematically shown in Figure 1a by finite-difference time domain (FDTD) simulation. The substrate is silica and a

hexagonal array of Si nanodisks is formed on a flat Si thin film that acts as a conductive layer for the detection of photocurrent. The diameter (D) and height (h) of nanodisks are 700 and 50 nm, respectively, and the pitch (P) is 750 nm. The thickness of a Si film (t) is 110 nm. We calculate the transmittance (T) and the reflectance (R) under normal incidence and obtain the absorptance (A =1-T-R) in the wavelength range from 1000 nm to 1800 nm. Since the dispersion of the refractive index of Si is very small in the wavelength range, we use fixed values for the refractive index (n =3.5) and the extinction coefficient (κ =10^{-3}). Figure 1b shows the calculated transmittance and absorptance spectra. The reflectance spectrum is shown in the Supporting Information (Figure S1). In the transmittance spectrum, three sharp dips are seen around 1602, 1137, and 1050 nm. At the 1602 and 1050 nm dips, strong absorption peaks appear, despite the very small extinction coefficient (κ =10^{-3}). On the other hand, at the 1137 nm transmittance dip, the absorption peak is very small. This suggests that the origin of the 1137 nm transmittance dip is different from others.

Figure 1c-e shows the electric field distributions ($|\boldsymbol{E}|/|\boldsymbol{E_0}|$), where $|\boldsymbol{E_0}|$ is the electric field intensity of incident light, at z = 0 (xy-plane), x = 0 (yz-plane), and y = 0 (zx-plane) at 1602, 1137 and 1050 nm, respectively. Si regions are surrounded by thick broken lines. At 1602 nm (Figure 1c), we can see symmetric current loops characteristic of the TD mode. The strong absorption at the wavelength is thus due to the sub-radiant TD resonance[31]. We refer the peak from a conventional nomenclature to the TE_{110} mode, where the subscripts denote the number of nodes across azimuth, radial, and z directions. At this resonance, the electric field is strongly confined in the Si region below a Si nanodisk, despite the small disk height compared to the Si film thickness (h/t =0.46). This strong confinement of the electric field in the Si region brings about the strong light absorption. The maximum enhancement factor of the electric field reaches 10.3. The

absorption peak at 1050 nm is assigned to the radial higher-order TD mode.[34,40] From the field distribution in Figure 1e, we refer the high-order TD mode to the TE_{120} mode. The field is more tightly confined than the TE_{110} mode, and the enhancement factor reaches 17.3.

The origin of the transmittance dip at 1137 nm is different from the others. This is a Rayleigh anomaly arising from the formation of the periodic structure.[41,42] The electric field is enhanced mainly in the region between Si nanodisks (Figure 1d). As a result, the absorption enhancement is marginal, despite the deep transmittance dip (Figure 1b). The mode is assigned to the TM_{110} mode from the magnetic field distribution (Figure S2 in the Supporting Information).

The resonance wavelengths of these modes can be controlled by the structural parameters of nanodisks, *i.e.*, P, D and h [31], and by the thickness of a Si film (t). In particular, it is very sensitive to a Si film thickness. Figure 1f shows the contour plot of the absorptance spectra of Si nanodisk arrays formed on different thickness Si films. The structure of the nanodisk array is the same as that shown in Figure 1a. We can see that the resonance modes show significant red-shift with increasing the Si film thickness. The sensitiveness of the resonance wavelength on the Si film thickness arises from the fact that the electric field is predominantly distributed in the region of a Si film below the nanodisks due to the very small nanodisk height.

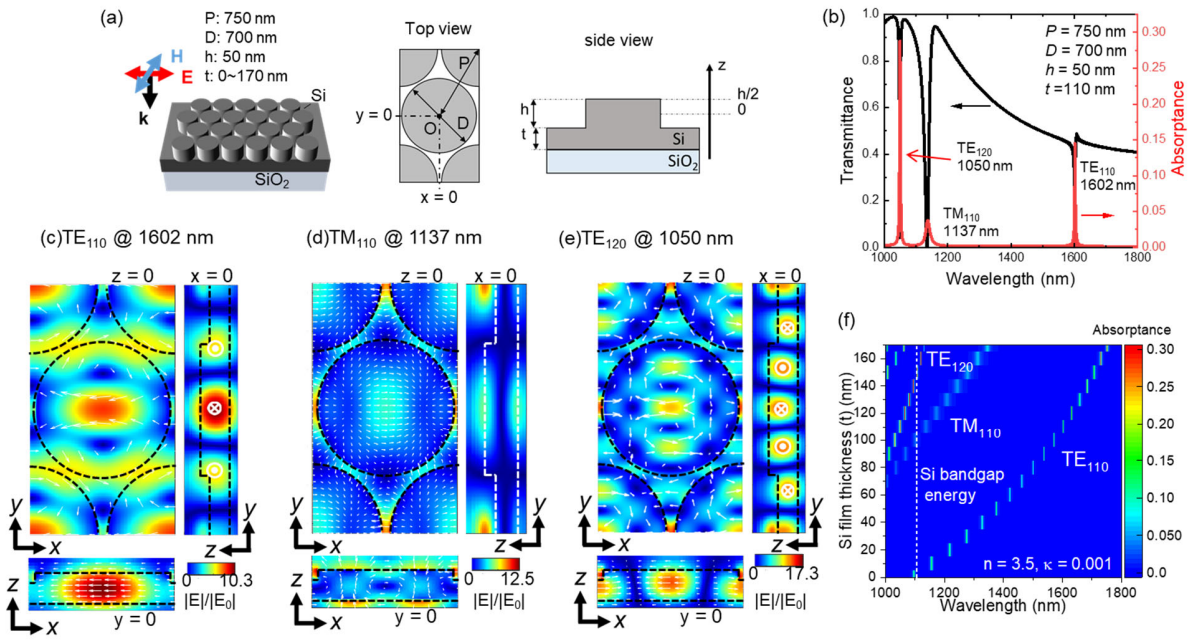

Figure 1. (a) (left) Schematic illustration of a Si nanodisk hexagonal array formed on a Si thin film. The directions of wavevector (*k*), electric field (*E*) and magnetic field (*H*) of incident light are also shown. (right) top and side views of Si nanodisk hexagonal array and the definition of structural parameters. (b) Calculated transmittance (black curve) and absorptance (red curve) spectra of Si nanodisk hexagonal array with $P = 750$ nm, $D = 700$ nm, $h = 50$ nm, and $t = 110$ nm. (c-e) Electric field distributions in *xy* (z =0), *yz* (x =0) and *xz* (y =0) planes at 1602 nm (TE_{110}) (c), 1137 nm (TM_{110}) (d) and 1050 nm (TE_{120}) (e). Dash lines surround Si regions. (f) Counter plot of absorptance spectra. The vertical axis is Si film thickness (t). Other structural parameters are fixed; P =750 nm, D =700 nm, and h =50 nm.

In the experiments described later, we use poly-Si films produced by annealing sputter-deposited amorphous Si for the preparation of nanodisk arrays. The poly-Si films are defective and there is defect-related weak absorption below the band gap. Typically, the extinction coefficient of

intrinsic poly-Si in the NIR range is ~10^{-2}. [20,21,43] Although it is better to use the extinction coefficient value determined by ellipsometry for numerical simulations, it is too low for the accurate measurement for thin films. Therefore, we simulate absorptance spectra by changing the extinction coefficient in a wide range (10^{-1} – 10^{-4}). Figure 2a shows the results. The peak wavelengths are not affected because of the fixed n, while the intensity and the width of the modes change depending on κ. Figure 2b and c shows the peak absorptance and the full-width half maximum (FWHM) of each mode as a function of κ obtained after subtracting the broad background absorption (Figure S3 in the Supporting Information). Interestingly, the absorptance does not increase monotonously with κ, but has the maximum at a certain κ. The extinction coefficient at the maximum absorptance for the TM_{110} mode is relatively large (κ =3.0 ×10^{-2}), while those of the TE_{110} and TE_{120} modes are very small, i.e., 1.5 × 10^{-3} and 4.0 × 10^{-3}, respectively. These behaviors can be explained by the coupled mode theory, in which the maximum absorptance is achieved when the material loss is equal to the radiation loss[24]. The radiation loss of the TM_{110} mode is relatively large as can be seen in the large FWHM at the low extinction coefficient range (e.g., κ = 1.0 ×10^{-4}) in Figure 2c. The large radiation loss results in the absorptance maximum at relatively large κ (=3.0 ×10^{-2}). On the other hand, the radiation loss of the TE_{110} and TE_{120} modes is very small as can be seen in the extremely small FWHMs at the low extinction coefficient range in Figure 2c. This brings the absorptance maximum to the very small extinction coefficient range (κ = 1.5 × 10^{-3} and 4.0 × 10^{-3}, respectively). In the Supporting Information, we quantitatively estimate the extinction coefficient at the maximum absorptance by the coupled mode theory and obtained good agreement with the values estimated from Figure 2b. Figure 2b and c indicates that very narrow absorption bands can be realized in the almost transparent wavelength range of Si by utilizing the TD resonances (TE_{110} and TE_{120} modes).

The relation between the peak absorptance and the extinction coefficient depends strongly on the structural parameter of the metasurface. As an example, we show the data when the Si film thickness (t) is 170 nm in the Supporting Information (Figure S5); other parameters are the same as those in Figure 2. In that case, the absorptance peak of the TE_{120} mode shifts to very small extinction coefficient range (κ_{max} : ~2.0×10^{-4}), while that of the TE_{110} mode is not strongly affected (κ_{max}: ~2.0×10^{-3}). The maximum absorptance of the TE_{110} mode increases from 0.15 in Figure 2b (t =110 nm) to 0.33, while the FWHM at the absorptance maxima is kept small. Therefore, the developed structure can be tuned to make the absorptance the largest for a desired extinction coefficient.

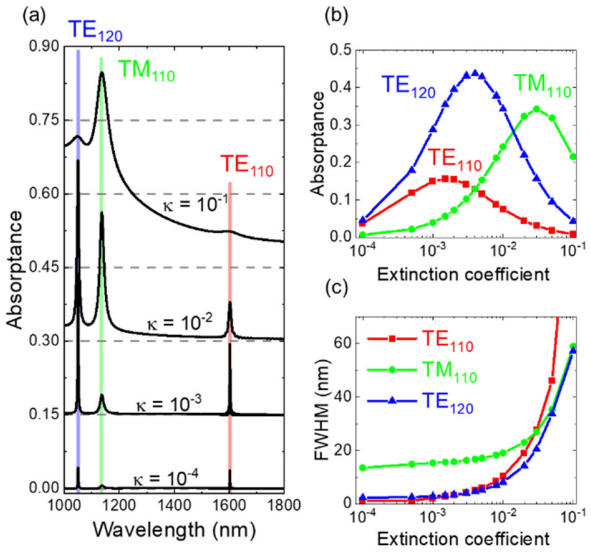

Figure 2. (a) Calculated absorptance spectra of Si nanodisk hexagonal arrays with P =750 nm, D =700 nm, h =50 nm and t =110 nm. The extinction coefficient is changed from 10^{-1} – 10^{-4}, while the refractive index is fixed to 3.5. (b) Absorptance values at the maximum of absorptance peaks as a function of extinction coefficients. (c) FWHM of absorptance peaks as a function of extinction coefficient.

Photoresponse of Si nanodisk hexagonal array

We employ nanosphere lithography to fabricate hexagonal arrays of Si nanodisks over a large area[31]. Details of the preparation procedure are described in the Method section. Figure 3a shows a scanning electron microscope (SEM) image of a produced Si hexagonal array. In this work, we fixed the pitch, diameter and height of Si nanodisks (P =710 nm, D =550 nm and h = 30 nm) and changed only the thickness of a Si film (t =20, 50, 70, 100 and 150 nm). The disk height (h) is estimated from the AFM image (Figure S6 in the Supporting information). On a nanodisk array, aluminum (Al) stripe electrodes are formed for the photocurrent measurement. Schematic illustrations of the photocurrent measurement setup and the energy band diagram are shown in Figure 3b. The distance between the electrodes is 200 μm. Figure 3c-g shows the transmittance and photocurrent (responsivity) spectra of the devices with t =20, 50, 70, 100 and 150 nm, respectively. The photocurrent spectra of flat Si thin films with the thickness of $t + h$ (= t + 30 nm) are also shown in each spectrum. We can see transmittance dips predicted by the simulations (TE_{110}, TM_{110}, and TE_{120} modes), although the width is larger than the simulations (see Figure S7 in the Supporting Information for the comparison of calculated and experimental transmittance spectra). The broadening is mainly due to partial disorder of the periodic structure, which is difficult to avoid in the nanosphere lithography process. The important fact is that, although broadened, clear transmittance dips appear in the sub-band gap wavelength range and the wavelength is well controlled by the Si film thickness.

In Figure 3c-g, at the wavelength of transmittance dips, we can clearly see photocurrent peaks. In the Supporting Information (Figure S7), we compare a measured responsivity spectrum with a calculated absorptance spectrum. Although the responsivity peaks are broader than the calculated absorptance peaks, the peak wavelengths agree very well. This indicates that the photocurrent

peaks arise from the absorption enhancement by the resonant modes and resultant increase of photogenerated carriers. The photocurrent is roughly proportional to the excitation power (Figure S8 in the Supporting Information). Figure 3h-l shows photocurrent enhancement factor spectra obtained by dividing photocurrent of a Si nanodisk hexagonal array with that of a flat Si film in Figure 3c-g, respectively. We can more clearly see photocurrent enhancement by the resonant modes. In the sub-band gap range of Si, the enhancement factor reaches ~30 (1300 nm in Figure 3k). Even at longer wavelengths, e.g., 1575 nm in Figure 3l, substantial photocurrent enhancement (~6) is observed. The FWHM of the peaks are around 30~60 nm, which is narrower than that reported in Si-based photodetectors using LSPRs of metal nanostructures[12,14]. The photocurrent spectra are independent of the polarization of incident light because of the symmetric structure (Figure S9 in the supporting Information).

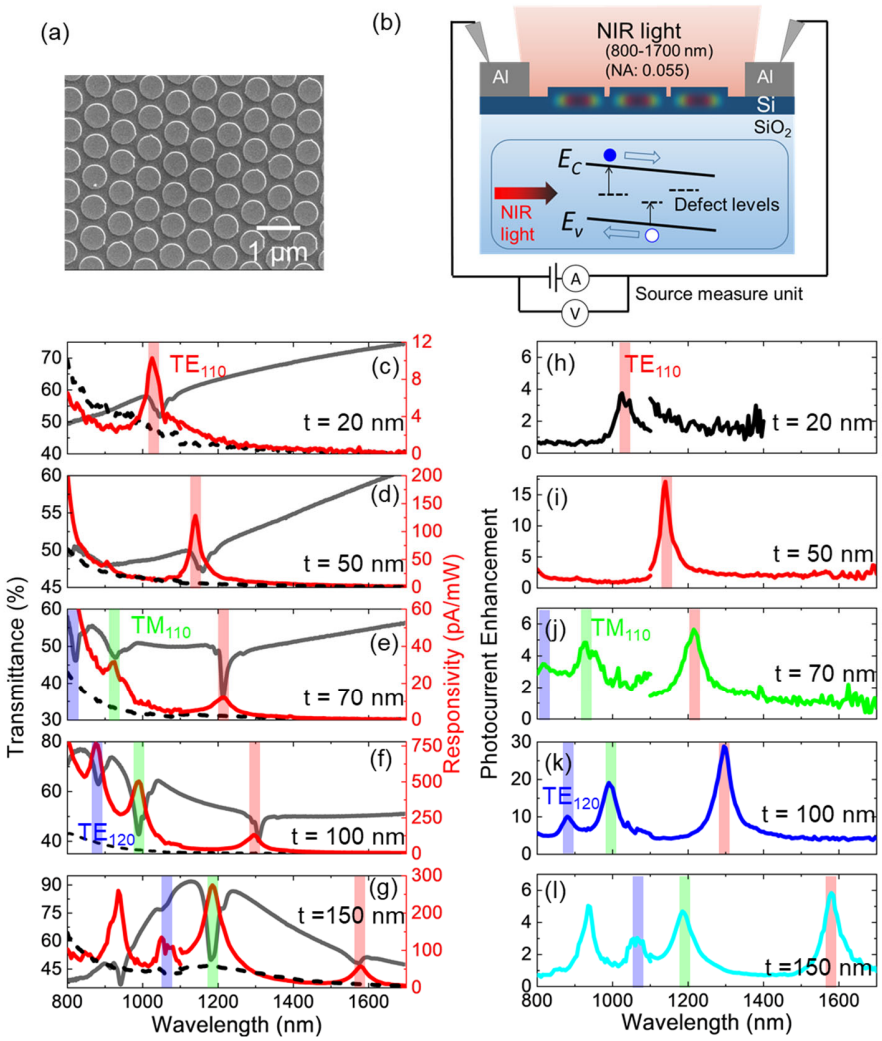

Figure 3. (a) SEM image of Si nanodisk hexagonal array (P =710 nm, D =550 nm, h =30 nm and t =150 nm). (b) Schematic illustration of the sample structure and the photocurrent measurement setup. Al electrodes are formed on a Si thin film on which a hexagonal array of Si nanodisks is formed. The substrate is silica. The DC current is measured by a source measure unit. The Si nanodisk hexagonal array is illuminated by monochromatized NIR light. In the image, schematic illustration of the energy band structure is also shown. E_c and E_v represent the conduction and valence band edges of Si, respectively. (c-g) Transmittance (gray line) and photocurrent (responsivity) (red) spectra of samples with different Si film thicknesses (t); (c) 20 nm, (d) 50 nm, (e) 70 nm, (f) 100 nm and (g) 150 nm. Other structural parameters are fixed (P =710 nm, D =550

nm and h =30 nm). Black broken curves are responsivity of flat Si films with the thicknesses of t + h (=t + 30 nm). (h-l) Photocurrent enhancement factor spectra obtained by dividing photocurrent of a Si nanodisk hexagonal array with that of a flat Si film in (c-g), respectively.

The narrow polarization-independent photocurrent peaks of the nanodisk arrays can be used for a current-detection type refractive index sensor operating in the NIR range. In contrast to conventional dielectric-metasurface-based refractive index sensors that monitor the intensity of the transmitted or reflected light by external NIR photodetectors [44–48], our device does not require the NIR photodetector. This may reduce the size and cost of the system, and potentially improve the sensitivity, especially in the wavelength where a conventional Si photodetector cannot be used. In order to simulate the effect of refractive index change, we place a thin dielectric layer (30 nm in thickness) with the refractive index of 1.0 (vacuum) to 1.6 on top of a Si nanodisk array and calculate the absorptance spectra. The structural parameters are P =710 nm, D =550 nm, h =30 nm, and t =100 nm. The refractive index of Si is set to 3.1. Figure 4a shows the calculated absorption spectra around the TE_{110} mode. The peak shifts to longer wavelength with increasing the refractive index. The sensitivity defined by $\Delta\lambda/\Delta n$ is approximately 29.6 nm/RIU. The peak absorptance and the FWHM change only slightly. The slight decrease of the FWHM, *i.e.*, from 2.6 to 2.1 nm, is due to the decrease of the radiation loss caused by the reduced refractive index contrast between the substrate and the surrounding medium.

In order to experimentally prove detection of a refractive index change by the photocurrent, we deposit a 30 nm thick polystyrene film (n =~1.59) on top of the device in Figure 3f by spin coating and measured the transmittance and photocurrent spectra. Figure 4b shows the results around the TE_{110} mode. Both the transmittance dip and the photocurrent peak shift to longer wavelength by

the polystyrene deposition. The photocurrent peak shifts 13 nm, which is close to the expected value (17.8 nm). Therefore, the TD resonances of a Si nanodisk array can be used as a current-detection type refractive index sensor.

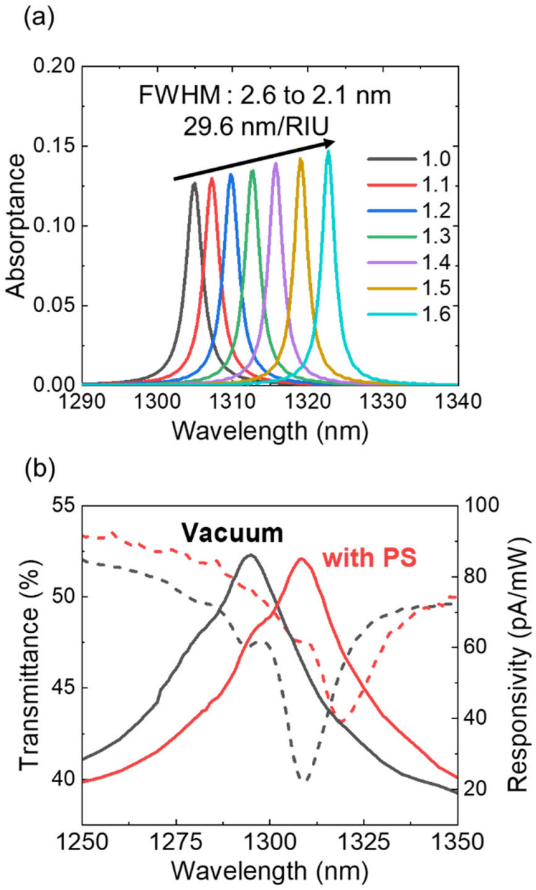

Figure 4. (a) Calculated absorption spectra of Si nanodisk hexagonal arrays (P =710 nm, D =550 nm, h =30 nm, and t =100 nm, n =3.1, κ =10^{-3}). A thin dielectric layer (30 nm in thickness) with the refractive index of 1.0 (vacuum) to 1.6 is placed on the top. (b) Measured transmittance (broken curves) and photocurrent spectra (solid curves) of a Si nanodisk hexagonal array with (red curves) and without a 30 nm thick polystyrene film (black curves).

Conclusion

The hexagonal array of Si nanodisks formed on a Si thin film possesses TD resonances that enhance light absorption in the sub-band gap wavelength region where the extinction coefficient is very small. We have demonstrated that the narrow-band absorption enhancement by the TD resonances can be utilized to enhance the photocurrent of a Si thin film in the sub-band gap wavelength range. We showed that the resonance wavelength can be controlled in a wide wavelength range and the photocurrent is at maximum ~30-fold enhanced at 1300 nm. We also showed that the photocurrent peaks shift depending on the refractive index of surrounding medium, and thus the device can be used as a current-detection type refractive index sensor operating in the sub-band gap wavelength range of Si.

Methods

Numerical Simulation: The FDTD simulations of a hexagonal array of Si nanodisks were carried out using a commercial software (Lumerical, Ansys). Since we focus our attention mainly on the long wavelength range below the bulk Si band gap, fixed values of the refractive index (3.1 - 3.5) and the extinction coefficients (10^{-1} – 10^{-4}) were used for the simulations. The refractive index of a SiO_2 substrate was set to 1.46, and the thickness is assumed to be infinite. The periodic boundary conditions were used for the *x*- and *y*-directions and the perfectly matched layer (PML) boundary was used for the *z*-direction. The structure was illuminated by a plane wave polarized along the *x*-axis in Figure 1a from the normal to the surface. Transmission and reflection spectra were obtained by 2D power monitors.

Fabrication of silicon nanodisk hexagonal arrays: The fabrication procedure is shown in our previous paper[31]. Amorphous Si films 50 - 180 nm in thickness were deposited on a SiO_2 substrate 750 μm in thickness by an rf-sputtering apparatus (ANELVA: SPF-210H). The Ar flow rate, the

total pressure, and the sputtering power were 20 sccm, 20 mTorr and 100 W, respectively. A monolayer of polystyrene beads (PSBs) (Polysciences Inc.) with the diameter of 750 nm was deposited on a Si film as an etching mask. The diameter of PSBs, i.e., the mask size, was controlled by oxygen plasma RIE (ANELVA: L-201D). The PSB mask pattern was transferred to a Si film by Ar^+ etching. The PSB mask was then removed by N,N-Dimethylformamide (FUJIFILM Wako). Finally, Si ND arrays were annealed at 800ºC in a N_2 atmosphere for an hour for the crystallization. The refractive index of Si films measured after the crystallization annealing was 3.1 - 3.5 at 1000 nm.

Al electrodes for photocurrent measurements (10 mm in length, 400 μm in width and 150 nm in thickness) were deposited by vacuum deposition after removing the native oxide by hydrofluoric acid etching. After the deposition, the samples were sintered at 600ºC for 10 min in a N_2 atmosphere.

Transmittance and photocurrent measurements: Transmittance spectra of nanodisk arrays were measured by a double-beam spectrophotometer (Shimadzu, UV-3101PC). The incident light was randomly polarized. For the photocurrent measurements, a nanodisk array was illuminated from the normal through an objective lens (N.A. =0.055). The light source was a supercontinuum laser (NKT Photonics, SuperK EVO) monochronized by an acousto-optic tunable filter (NKT Photonics, SuperK SELECT NIR 1 for 800 to 1100 nm and SUPERK SELECT IR for 1100 to 1700 nm). Current was measured with a source measurement unit (Keithley 236) under the applied bias of 100 V. Photocurrent measurements were carried out in vacuum.

ASSOCIATED CONTENT

Supporting Information. The following files are available free of charge.

Calculated reflectance spectrum of Si nanodisk hexagonal array; magnetic field distributions at the resonances in Fig.1; estimation of the peak absorptance value and the full width half maximum; estimation of optimum extinction coefficients for maximum absorptance; AFM image of the Si nanodisk array in Fig. 3a; comparison of measured and calculated transmittance spectra; comparison of calculated absorptance spectrum and measured photocurrent spectrum; photocurrent intensity as a function of excitation power; photocurrent spectra at different polarization direction of incident light (PDF)

AUTHOR INFORMATION

Corresponding Authors

Minoru Fujii
Department of Electrical and Electronic Engineering, Graduate School of Engineering, Kobe University, Rokkodai, Nada, Kobe 657-8501, Japan
E-mail: fujii@eedept.kobe-u.ac.jp

Hiroshi Sugimoto
Department of Electrical and Electronic Engineering, Graduate School of Engineering, Kobe University, Rokkodai, Nada, Kobe 657-8501, Japan
E-mail: sugimoto@eedept.kobe-u.ac.jp

Authors

Hiroaki Hasebe
Department of Electrical and Electronic Engineering, Graduate School of Engineering, Kobe University, Rokkodai, Nada, Kobe 657-8501, Japan

Keisuke Moriasa
Department of Electrical and Electronic Engineering, Graduate School of Engineering, Kobe University, Rokkodai, Nada, Kobe 657-8501, Japan

Kaito Yamashita
Department of Electrical and Electronic Engineering, Graduate School of Engineering, Kobe University, Rokkodai, Nada, Kobe 657-8501, Japan

Author Contributions

The manuscript was written through the contributions of all authors. All authors have given approval to the final version of the manuscript.

ACKNOWLEDGMENT

This work is partly supported also by JSPS KAKENHI Grant Numbers 18KK0141, 21H01748, 21H01782 and 21K14496.

REFERENCES

(1) Bünzli, J. C. G.; Eliseeva, S. V. Lanthanide NIR Luminescence for Telecommunications, Bioanalyses and Solar Energy Conversion. *J. Rare Earths* **2010**, *28* (6), 824–842. https://doi.org/10.1016/S1002-0721(09)60208-8.

(2) Ijaz, M.; Ghassemlooy, Z.; Rajbhandari, S.; Le Minh, H.; Perez, J.; Gholami, A. Comparison of 830 Nm and 1550 Nm Based Free Space Optical Communications Link under Controlled Fog Conditions. In *Proceedings of the 2012 8th International Symposium on Communication Systems, Networks and Digital Signal Processing, CSNDSP 2012*; 2012. https://doi.org/10.1109/CSNDSP.2012.6292739.

(3) Yamada, H.; Chu, T.; Ishida, S.; Arakawa, Y. Si Photonic Wire Waveguide Devices. *IEEE J. Sel. Top. Quantum Electron.* **2006**, *12* (6), 1371–1378. https://doi.org/10.1109/JSTQE.2006.880611.

(4) Kaushal, H.; Kaddoum, G. Optical Communication in Space: Challenges and Mitigation Techniques. *IEEE Communications Surveys and Tutorials*. 2017, pp 57–96. https://doi.org/10.1109/COMST.2016.2603518.

(5) Du, H.; Shi, H.; Liu, Y.; Zeng, D.; Mei, T. Towards NIR-VIS Masked Face Recognition. *IEEE Signal Process. Lett.* **2021**, *28*, 768–772. https://doi.org/10.1109/LSP.2021.3071663.

(6) He, R.; Wu, X.; Sun, Z.; Tan, T. Wasserstein CNN: Learning Invariant Features for NIR-VIS Face Recognition. *IEEE Trans. Pattern Anal. Mach. Intell.* **2019**, *41* (7), 1761–1773. https://doi.org/10.1109/TPAMI.2018.2842770.

(7) He, Q.; Lou, M.; Zheng, C.; Ye, W.; Wang, Y.; Tittel, F. K. Repetitively Mode-Locked Cavity-Enhanced Absorption Spectroscopy (RML-CEAS) for near-Infrared Gas Sensing. *Sensors (Switzerland)* **2017**, *17* (12), 2792. https://doi.org/10.3390/s17122792.

(8) Escobedo, J. O.; Rusin, O.; Lim, S.; Strongin, R. M. NIR Dyes for Bioimaging Applications. *Curr. Opin. Chem. Biol.* **2010**, *14* (1), 64–70. https://doi.org/10.1016/j.cbpa.2009.10.022.

(9) Li, Y.; Liu, Y.; Li, Q.; Zeng, X.; Tian, T.; Zhou, W.; Cui, Y.; Wang, X.; Cheng, X.; Ding, Q.; Wang, X.; Wu, J.; Deng, H.; Li, Y.; Meng, X.; Deng, Z.; Hong, X.; Xiao, Y. Novel NIR-II Organic Fluorophores for Bioimaging beyond 1550 Nm. *Chem. Sci.* **2020**, *11* (10), 2621–2626. https://doi.org/10.1039/c9sc06567a.

(10) Hong, G.; Antaris, A. L.; Dai, H. Near-Infrared Fluorophores for Biomedical Imaging. *Nat. Biomed. Eng.* **2017**, *1* (1), 1–22. https://doi.org/10.1038/s41551-016-0010.

(11) Knight, M. W.; Sobhani, H.; Nordlander, P.; Halas, N. J. Photodetection with Active Optical Antennas. *Science (80-.).* **2011**, *332* (6030), 702–704. https://doi.org/10.1126/science.1203056.

(12) Tanzid, M.; Ahmadivand, A.; Zhang, R.; Cerjan, B.; Sobhani, A.; Yazdi, S.; Nordlander,

P.; Halas, N. J. Combining Plasmonic Hot Carrier Generation with Free Carrier Absorption for High-Performance Near-Infrared Silicon-Based Photodetection. *ACS Photonics* **2018**, *5* (9), 3472–3477. https://doi.org/10.1021/acsphotonics.8b00623.

(13) Sobhani, A.; Knight, M. W.; Wang, Y.; Zheng, B.; King, N. S.; Brown, L. V.; Fang, Z.; Nordlander, P.; Halas, N. J. Narrowband Photodetection in the Near-Infrared with a Plasmon-Induced Hot Electron Device. *Nat. Commun.* **2013**, *4* (1), 1–6. https://doi.org/10.1038/ncomms2642.

(14) Li, W.; Valentine, J. Metamaterial Perfect Absorber Based Hot Electron Photodetection. *Nano Lett.* **2014**, *14* (6), 3510–3514. https://doi.org/10.1021/nl501090w.

(15) Cao, J.; Sun, T.; Grattan, K. T. V. Gold Nanorod-Based Localized Surface Plasmon Resonance Biosensors: A Review. *Sensors and Actuators, B: Chemical*. Elsevier B.V. 2014, pp 332–351. https://doi.org/10.1016/j.snb.2014.01.056.

(16) Logan, D. F.; Knights, A. P.; Jessop, P. E.; Tarr, N. G. Defect-Enhanced Photo-Detection at 1550 Nm in a Silicon Waveguide Formed via LOCOS. *Semicond. Sci. Technol.* **2011**, *26* (4), 045009. https://doi.org/10.1088/0268-1242/26/4/045009.

(17) Fard, S. T.; Murray, K.; Caverley, M.; Donzella, V.; Flueckiger, J.; Grist, S. M.; Huante-Ceron, E.; Schmidt, S. A.; Kwok, E.; Jaeger, N. A. F.; Knights, A. P.; Chrostowski, L. Silicon-on-Insulator Sensors Using Integrated Resonance-Enhanced Defect-Mediated Photodetectors. *Opt. Express* **2014**, *22* (23), 28517. https://doi.org/10.1364/oe.22.028517.

(18) Bradley, J. D. B.; Jessop, P. E.; Knights, A. P. Silicon Waveguide-Integrated Optical Power Monitor with Enhanced Sensitivity at 1550 Nm. *Appl. Phys. Lett.* **2005**, *86* (24), 1–3. https://doi.org/10.1063/1.1947379.

(19) Garín, M.; Fenollosa, R.; Alcubilla, R.; Shi, L.; Marsal, L. F.; Meseguer, F. All-Silicon

Spherical-Mie-Resonator Photodiode with Spectral Response in the Infrared Region. *Nat. Commun.* **2014**, *5* (1), 3440. https://doi.org/10.1038/ncomms4440.

(20) Reiter, S.; Koper, N.; Reineke-Koch, R.; Larionova, Y.; Turcu, M.; Krügener, J.; Tetzlaff, D.; Wietler, T.; Höhne, U.; Kähler, J. D.; Brendel, R.; Peibst, R. Parasitic Absorption in Polycrystalline Si-Layers for Carrier-Selective Front Junctions. In *Energy Procedia*; Elsevier, 2016; Vol. 92, pp 199–204. https://doi.org/10.1016/j.egypro.2016.07.057.

(21) Casalino, M.; Coppola, G.; De La Rue, R. M.; Logan, D. F. State-of-the-Art All-Silicon Sub-Bandgap Photodetectors at Telecom and Datacom Wavelengths. *Laser and Photonics Reviews*. John Wiley & Sons, Ltd November 1, 2016, pp 895–921. https://doi.org/10.1002/lpor.201600065.

(22) Tian, J.; Luo, H.; Li, Q.; Pei, X.; Du, K.; Qiu, M. Near-Infrared Super-Absorbing All-Dielectric Metasurface Based on Single-Layer Germanium Nanostructures. *Laser Photonics Rev.* **2018**, *12* (9), 1800076. https://doi.org/10.1002/lpor.201800076.

(23) Fan, S.; Suh, W.; Joannopoulos, J. D. Temporal Coupled-Mode Theory for the Fano Resonance in Optical Resonators. *J. Opt. Soc. Am. A* **2003**, *20* (3), 569. https://doi.org/10.1364/josaa.20.000569.

(24) Piper, J. R.; Liu, V.; Fan, S. Total Absorption by Degenerate Critical Coupling. *Appl. Phys. Lett.* **2014**, *104* (25), 251110. https://doi.org/10.1063/1.4885517.

(25) Tian, J.; Li, Q.; Belov, P. A.; Sinha, R. K.; Qian, W.; Qiu, M. High- Q All-Dielectric Metasurface: Super and Suppressed Optical Absorption. *ACS Photonics* **2020**, *7* (6), 1436–1443. https://doi.org/10.1021/acsphotonics.0c00003.

(26) Yang, C. Y.; Yang, J. H.; Yang, Z. Y.; Zhou, Z. X.; Sun, M. G.; Babicheva, V. E.; Chen, K. P. Nonradiating Silicon Nanoantenna Metasurfaces as Narrowband Absorbers. *ACS*

Photonics **2018**, *5* (7), 2596–2601. https://doi.org/10.1021/acsphotonics.7b01186.

(27) Xu, R.; Takahara, J. All-Dielectric Perfect Absorber Based on Quadrupole Modes. *Opt. Lett.* **2021**, *46* (15), 3596. https://doi.org/10.1364/ol.431398.

(28) Miroshnichenko, A. E.; Evlyukhin, A. B.; Yu, Y. F.; Bakker, R. M.; Chipouline, A.; Kuznetsov, A. I.; Luk'yanchuk, B.; Chichkov, B. N.; Kivshar, Y. S. Nonradiating Anapole Modes in Dielectric Nanoparticles. *Nat. Commun.* **2015**, *6*, 1–8. https://doi.org/10.1038/ncomms9069.

(29) Parker, J. A.; Sugimoto, H.; Coe, B.; Eggena, D.; Fujii, M.; Scherer, N. F.; Gray, S. K.; Manna, U. Excitation of Nonradiating Anapoles in Dielectric Nanospheres. *Phys. Rev. Lett.* **2020**, *124* (9). https://doi.org/10.1103/PhysRevLett.124.097402.

(30) Hüttenhofer, L.; Tittl, A.; Kühner, L.; Cortés, E.; Maier, S. A. Anapole-Assisted Absorption Engineering in Arrays of Coupled Amorphous Gallium Phosphide Nanodisks. *ACS Photonics* **2021**, *8* (5), 1469–1476. https://doi.org/10.1021/acsphotonics.1c00238.

(31) Hasebe, H.; Sugimoto, H.; Hinamoto, T.; Fujii, M. Coupled Toroidal Dipole Modes in Silicon Nanodisk Metasurface: Polarization Independent Narrow Band Absorption and Directional Emission. *Adv. Opt. Mater.* **2020**, *8* (22). https://doi.org/10.1002/adom.202001148.

(32) Xu, L.; Rahmani, M.; Zangeneh Kamali, K.; Lamprianidis, A.; Ghirardini, L.; Sautter, J.; Camacho-Morales, R.; Chen, H.; Parry, M.; Staude, I.; Zhang, G.; Neshev, D.; Miroshnichenko, A. E. Boosting Third-Harmonic Generation by a Mirror-Enhanced Anapole Resonator. *Light Sci. Appl.* **2018**, *7* (1). https://doi.org/10.1038/s41377-018-0051-8.

(33) Timofeeva, M.; Lang, L.; Timpu, F.; Renaut, C.; Bouravleuv, A.; Shtrom, I.; Cirlin, G.;

Grange, R. Anapoles in Free-Standing III-V Nanodisks Enhancing Second-Harmonic Generation. *Nano Lett.* **2018**, *18* (6), 3695–3702. https://doi.org/10.1021/acs.nanolett.8b00830.

(34) Grinblat, G.; Li, Y.; Nielsen, M. P.; Oulton, R. F.; Maier, S. A. Efficient Third Harmonic Generation and Nonlinear Subwavelength Imaging at a Higher-Order Anapole Mode in a Single Germanium Nanodisk. *ACS Nano* **2017**, *11* (1), 953–960. https://doi.org/10.1021/acsnano.6b07568.

(35) Baranov, D. G.; Verre, R.; Karpinski, P.; Käll, M. Anapole-Enhanced Intrinsic Raman Scattering from Silicon Nanodisks. *ACS Photonics* **2018**, *5* (7), 2730–2736. https://doi.org/10.1021/acsphotonics.8b00480.

(36) Zhang, T.; Che, Y.; Chen, K.; Xu, J.; Xu, Y.; Wen, T.; Lu, G.; Liu, X.; Wang, B.; Xu, X.; Duh, Y. S.; Tang, Y. L.; Han, J.; Cao, Y.; Guan, B. O.; Chu, S. W.; Li, X. Anapole Mediated Giant Photothermal Nonlinearity in Nanostructured Silicon. *Nat. Commun.* **2020**, *11* (1), 1–9. https://doi.org/10.1038/s41467-020-16845-x.

(37) Totero Gongora, J. S.; Miroshnichenko, A. E.; Kivshar, Y. S.; Fratalocchi, A. Anapole Nanolasers for Mode-Locking and Ultrafast Pulse Generation. *Nat. Commun.* **2017**, *8*. https://doi.org/10.1038/ncomms15535.

(38) Hüttenhofer, L.; Eckmann, F.; Lauri, A.; Cambiasso, J.; Pensa, E.; Li, Y.; Cortés, E.; Sharp, I. D.; Maier, S. A. Anapole Excitations in Oxygen-Vacancy-Rich TiO2- x Nanoresonators: Tuning the Absorption for Photocatalysis in the Visible Spectrum. *ACS Nano* **2020**, *14* (2), 2456–2464. https://doi.org/10.1021/acsnano.9b09987.

(39) Hüttenhofer, L.; Golibrzuch, M.; Bienek, O.; Wendisch, F. J.; Lin, R.; Becherer, M.; Sharp, I. D.; Maier, S. A.; Cortés, E. Metasurface Photoelectrodes for Enhanced Solar Fuel

Generation. *Adv. Energy Mater.* **2021**, *11* (46), 2102877. https://doi.org/10.1002/aenm.202102877.

(40) Zenin, V. A.; Evlyukhin, A. B.; Novikov, S. M.; Yang, Y.; Malureanu, R.; Lavrinenko, A. V.; Chichkov, B. N.; Bozhevolnyi, S. I. Direct Amplitude-Phase Near-Field Observation of Higher-Order Anapole States. *Nano Lett.* **2017**, *17* (11), 7152–7159. https://doi.org/10.1021/acs.nanolett.7b04200.

(41) Castellanos, G. W.; Bai, P.; Gómez Rivas, J. Lattice Resonances in Dielectric Metasurfaces. *J. Appl. Phys.* **2019**, *125* (21). https://doi.org/10.1063/1.5094122.

(42) Babicheva, V. E. Lattice Effect in Mie-Resonant Dielectric Nanoparticle Array under Oblique Light Incidence. *MRS Commun.* **2018**, *8* (4), 1455–1462. https://doi.org/10.1557/mrc.2018.216.

(43) Fan, H. Y.; Ramdas, A. K. Infrared Absorption and Photoconductivity in Irradiated Silicon. *J. Appl. Phys.* **1959**, *30* (8), 1127–1134. https://doi.org/10.1063/1.1735282.

(44) Yesilkoy, F.; Arvelo, E. R.; Jahani, Y.; Liu, M.; Tittl, A.; Cevher, V.; Kivshar, Y.; Altug, H. Ultrasensitive Hyperspectral Imaging and Biodetection Enabled by Dielectric Metasurfaces. *Nature Photonics*. Nature Publishing Group June 1, 2019, pp 390–396. https://doi.org/10.1038/s41566-019-0394-6.

(45) Tseng, M. L.; Jahani, Y.; Leitis, A.; Altug, H. Dielectric Metasurfaces Enabling Advanced Optical Biosensors. *ACS Photonics*. 2021, pp 47–60. https://doi.org/10.1021/acsphotonics.0c01030.

(46) Wang, J.; Kühne, J.; Karamanos, T.; Rockstuhl, C.; Maier, S. A.; Tittl, A. All-Dielectric Crescent Metasurface Sensor Driven by Bound States in the Continuum. *Adv. Funct. Mater.* **2021**, *31* (46). https://doi.org/10.1002/adfm.202104652.

(47) Jeong, J.; Goldflam, M. D.; Campione, S.; Briscoe, J. L.; Vabishchevich, P. P.; Nogan, J.; Sinclair, M. B.; Luk, T. S.; Brener, I. High Quality Factor Toroidal Resonances in Dielectric Metasurfaces. *ACS Photonics* **2020**, *7* (7), 1699–1707. https://doi.org/10.1021/acsphotonics.0c00179.

(48) Algorri, J. F.; Zografopoulos, D. C.; Ferraro, A.; García-Cámara, B.; Beccherelli, R.; Sánchez-Pena, J. M. Ultrahigh-Quality Factor Resonant Dielectric Metasurfaces Based on Hollow Nanocuboids. *Opt. Express* **2019**, *27* (5), 6320. https://doi.org/10.1364/oe.27.006320.

For Table of Contents Use only

Title : Toroidal dipole-induced photocurrent enhancement in Si nanodisk hexagonal array below the band gap

Authors : Hiroaki Hasebe, Keisuke Moriasa, Kaito Yamashita, Hiroshi Sugimoto, Minoru Fujii

Synopsis : A hexagonal array of low-aspect-ratio silicon nanodisks for narrowband photocurrent enhancement in the sub-band gap wavelength range.